Atmos. Chem. Phys. Discuss., 11, 31159–31206, 2011
www.atmos-chem-phys-discuss.net/11/31159/2011/
doi:10.5194/acpd-11-31159-2011

Atmospheric Chemistry and Physics Discussions

Satellite climatology of cloud liquid water path over the Southeast Pacific between 2002 and 2009

L. W. O'Neill[1,*], **S. Wang**[2], **and Q. Jiang**[2]

[1]Naval Research Laboratory/National Research Council, Monterey, CA, USA
[2]Marine Meteorology Division, Naval Research Laboratory, Monterey, CA, USA
[*]now at: College of Oceanic and Atmospheric Sciences, Oregon State University, Corvallis, OR, USA

Received: 23 August 2011 – Accepted: 2 September 2011 – Published: 25 November 2011

Correspondence to: L. W. O'Neill (loneill@coas.oregonstate.edu)

Published by Copernicus Publications on behalf of the European Geosciences Union.

Abstract

Spatial and temporal variability of liquid water path (LWP) over the southeast Pacific is described using LWP observations made by four satellite microwave radiometers (Advanced Microwave Scanning Radiometer on EOS-Aqua (AMSR-E), Tropical Rainfall Measuring Mission Microwave Imager (TMI), and the Special Sensor Microwave Imager (SSM/I) F13 and F15 satellites) for the 7-yr period June 2002–May 2009. This study quantifies seasonal and interannual variability of the LWP and LWP diurnal and semi-diurnal cycles at 30-day intervals during the 7-yr analysis period. The LWP field shows considerable spatial and seasonal variability throughout the southeast Pacific, particularly associated with the southern branch of the Intertropical Convergence Zone (SITCZ) and the Southeast Pacific Convergence Zone (SPCZ). Two distinct annual cycles of LWP are apparent, both of which peak during the austral autumn. One is associated with an active phase of the SITCZ, while the other is associated with increased LWP in the SITCZ, SPCZ, and near coastal zones, and decreased LWP elsewhere. Consistent with previous observations, the LWP diurnal cycle peaks during the early morning and has the largest amplitude in a broad region near 85° W, 20° S. The amplitude of the LWP diurnal cycle exhibits a strong annual cycle which peaks during the austral summer. A secondary annual cycle in the LWP diurnal cycle amplitude peaks during the austral autumn south of 20° S and is a minimum within a zonal band between 8° S and 20° S. Finally, although this satellite combination barely resolves semi-diurnal LWP variability, it is shown that a statistically significant semi-diurnal cycle of LWP occurs off Peru and northern Chile, consistent with previous analyses. The amplitude of the LWP semidiurnal cycle tends to peak during the austral spring.

1 Introduction

Marine stratiform clouds frequently occupy large fractions of the sky over the southeast Pacific Ocean in the form of stratus, stratocumulus, and organized shallow cumulus. Closer to the equator, the cloud field transitions from shallow stratiform to that

ACPD
11, 31159–31206, 2011

associated with deep convection. The clouds' higher albedo compared to the ocean surface significantly alters the incoming shortwave radiation to the ocean; the reduction of incoming solar energy is compensated partially by increased downward longwave flux from the relatively warm, low-level clouds (e.g., Klein and Hartmann, 1993). Even though this area of the ocean is geographically remote, the radiative forcing by the extensive cloud deck makes a significant contribution to both regional and global climate. Unfortunately, coupled climate model simulations show a strong sensitivity to the clouds in this region, and yet realistic representation of these clouds remains one of the most challenging issues in climate modeling. For instance, persistent warm biases of ocean near-surface temperatures in these simulations have been attributed partly to biases in the models' cloud cover over the southeast Pacific (e.g., Mechoso et al., 1995; Ma et al., 1996; de Szoeke et al., 2010). Recent evaluations of numerical simulations and forecasts have concluded that numerical weather prediction models insufficiently simulate major aspects of the spatio-temporal variability of the southeast Pacific stratiform cloud deck, including diurnal variability and the mean state, compared to observations (e.g., de Szoeke et al., 2006; Hannay et al., 2009; Wyant et al., 2010; Wang et al., 2011).

Motivated by the importance of the cloud field for regional and global climate, a climatology of vertically-integrated cloud liquid water path (LWP) based on a combination of four microwave radiometers is used to characterize the dominant modes of spatial and temporal variability of LWP over the southeast Pacific Ocean (shown in Fig. 1c) during the 7-yr period June 2002–May 2009. These satellite observations can be used, for instance, to test the quantitative ability of numerical weather prediction and climate models to accurately simulate the cloud fields in the southeast Pacific, as has been done in Wyant et al. (2010) and Wang et al. (2011). Additionally, this climatology can be used to further investigate the dynamics, microphysical processes, and large-scale forcings that contribute to the spatio-temporal variability of the stratiform cloud deck in this region.

ACPD
11, 31159–31206, 2011

A focus of this analysis is to provide satellite observations of LWP in support of VOCALS-REx (VAMOS Ocean Cloud-Atmosphere-Land Study Regional Experiment). VOCALS-REx took place during between October and November 2008 and provided a wealth of in situ and remote observations to investigate and characterize the coupled climate system of the southeast Pacific Ocean. Clouds were a major focus for VOCALS-REx, given the plethora of interactions between them and several other aspects of the climate system. These satellite observations complement the wealth of in situ observational data obtained during VOCALS-REx over much longer temporal and larger spatial scales. Additionally, they have been used to provide quantitative assessments of LWP for the numerical modeling component of VOCALS, designated as VOCALS-Mod.

The diurnal cycle of the low-level stratiform cloud deck is a significant mode of variability in the southeast Pacific (e.g., Minnis and Harrison, 1984; Zuidema and Hartmann, 1995; Rozendaal et al., 1995; Wood et al., 2002; Garreaud and Muñoz, 2004; O'Dell et al., 2008). Additionally, diurnal variations of clouds have a considerable influence on the surface radiative budget (e.g., Rozendaal et al., 1995; Bergman and Salby, 1997). Through investigation of a number of cloud-related variables, these studies all conclude a large amplitude diurnal cycle in cloud thickness, coverage, and liquid water content over the southeast Pacific that reaches a maximum in the early morning and minimum in the afternoon. The stratiform cloud field over the southeast Pacific also shares similar diurnal variability with other eastern boundary current regions (e.g., Minnis et al., 1984; Bretherton et al., 1995; Rozendaal et al., 1995; Wood et al., 2002; O'Dell et al., 2008).

One of the earliest investigations of diurnal variability of LWP over the southeast Pacific was Zuidema and Hartmann (1995), who estimated LWP diurnal variability from differences in the morning and afternoon passes of the SSM/I F8 satellite. Wood et al. (2002) used LWP observations from the TMI equatorward of 40° to estimate the LWP diurnal cycle amplitude and phase on a 2.5° latitude by 2.5° longitude grid at approximately 2-month intervals. O'Dell et al. (2008) developed a global LWP climatology

ACPD
11, 31159–31206, 2011

based on 18 yr of LWP measurements from 8 passive microwave radiometers that operated during portions of the period January 1988–December 2005. As part of the climatology, they estimated the mean LWP diurnal and semidiurnal cycles on a 1° latitude by 1° longitude spatial grid at monthly intervals.

This study expands upon these previous studies in several ways. First, this analysis is focused exclusively on the SEP, thus providing a more in-depth description of the LWP variability there; second, we estimated variability of the LWP and LWP diurnal and semi-diurnal cycles on seasonal and longer timescales, which is accomplished through empirical orthogonal function (EOF) analysis of the LWP mean and diurnal and semi-diurnal cycle amplitudes at 30-day intervals over the 7-yr analysis period; and third, we computed the regressions on a 0.25° latitude by 0.25° longitude spatial grid, providing improved information on the spatial variability of the LWP and LWP diurnal and semi-diurnal cycles.

The satellite observations of LWP are discussed in detail in Sect. 2, including the accuracy of the satellite retrievals of LWP and the sampling characteristics of the four-satellite combination used in this analysis. The 7-yr mean state of the LWP in the southeast Pacific and the mean LWP diurnal cycle from these satellite observations are shown in Sect. 3. Spatial and temporal variability of the mean LWP field and diurnal cycle over the 7-yr analysis period is described in Sect. 4 through use of EOF analysis. LWP variability during the VOCALS-REx period 20 October–30 November 2008 is investigated in Sect. 5. Here, the LWP and diurnal cycle during the VOCALS-REx period is compared with the same days during the 6 previous years and with the 7-yr means shown in Sect. 3. In Sect. 6, an estimate of the LWP semi-diurnal cycle amplitude and phase is shown, along with an analysis of the seasonal variability of its amplitude. We close in Sect. 7 with our main conclusions and discussion of the results.

ACPD
11, 31159–31206, 2011

2 Data description and methods

2.1 Satellite dataset description

LWP integrated over the depth of the atmosphere over the ocean was estimated from four satellite passive microwave radiometers: the Tropical Rainfall Measuring Mission (TRMM) Microwave Imager (TMI); the Special Sensor Microwave Imager (SSM/I) on the Defense Meteorological Satellite Program (DMSP) F13 and F15 satellites; and the Advanced Microwave Scanning Radiometer on the Earth Observing System (EOS)-Aqua (AMSR-E) satellite. These satellites operated simultaneously during the 7-yr period 1 June 2002–31 May 2009, as shown by the timeline of each satellites' geophysical data record in Fig. 1a. Currently, all satellites are operational except for the SSM/I F13, which suffered a recorder malfunction on 18 November 2009 that ceased its observational capabilities. This four satellite combination provided continuous temporal coverage during this 7-yr period. Remote Sensing Systems (RSS) produced the satellite LWP datasets used here, which were gridded onto a uniform 0.25° spatial grid separately for ascending and descending swaths. The RSS dataset versions used were the latest versions at the completion of this analysis: version 4 for TMI; version 6 for the two SSM/I's; and version 5 for AMSR-E.

The passive microwave radiometers on these satellites provide measurements of the thermal emission of cloud droplets using a combination of brightness temperature measurements at several frequencies. Both the TMI and AMSR-E have additional low frequency channels that allow for retrieval of sea surface temperature (SST). Besides these low frequency channels, brightness temperatures at five channels are used for the retrieval of LWP for all instruments used here, which include vertical and horizontal polarizations at frequencies of 19 and 37 GHz, and vertical polarization at 22 GHz. The 19 GHz frequency provides the most sensitive estimate of LWP for large water droplets indicative of raining or drizzling clouds, while the 37 GHz channel is most sensitive to LWP for non-precipitating clouds with much smaller liquid water droplets. Brightness temperatures at 85 GHz are not used in the RSS version of the retrieval algorithm due

ACPD
11, 31159–31206, 2011

to its sensitivity to scattering of microwave radiation by large frozen particles (e.g., Liu and Curry, 1993). The retrieval algorithm used to generate estimates of LWP is nearly identical for each instrument used here, except for small differences in viewing geometry, sensor resolution, frequency, and sensor calibration between each satellite.

A recent in-depth discussion of microwave LWP retrieval methodology and uncertainty is given in Sects. 2 and 4 of O'Dell et al. (2008) and references therein. Briefly, one of the main sources of uncertainty in the passive microwave retrieval of LWP pertains to the partitioning of liquid water between cloud droplets and precipitation. This uncertainty is most prominent in regions of significant precipitation rates. Estimates of the normalized systematic uncertainties in the LWP retrieval due to cloud-rain separation are below 10 % over the southeast Pacific, as shown by Fig. 5a in O'Dell et al. (2008). The uncertainties become more significant approaching the equator and toward mid-latitudes, where precipitation is both more common and widespread. The relative smallness of this effect over the southeast Pacific is due to the lack of moderate to heavy precipitation there, and thus is not a significant concern for this analysis.

Another noteworthy source of uncertainty includes scattering of upwelled microwave radiation emitted by frozen particles larger than about 150 µm, which can significantly affect the brightness temperatures at 19 and 37 GHz independent of liquid water content (e.g., Liu and Curry, 1993). Fortunately, this effect is likely small in the southeast Pacific given the relative absense of frozen particles in the low-altitude stratiform cloud field and the relative infrequency of deep convection, mid-latitude frontal disturbances, and widespread cirrus. Near the equator and in the southern portions of the domain, this effect may be more significant, although the extent of potential uncertainties depends on detailed microphysical properties that are unfortunately difficult to estimate on the same spatial scales as the satellite observations.

ACPD
11, 31159–31206, 2011

2.2 Diurnal regression computation details

Diurnal regression estimates of LWP, denoted as $\widehat{L}$, are computed from the satellite LWP observations L at 30-day intervals over the 7-yr analysis period using

$$\widehat{L} = \widehat{\beta}_0 + \widehat{\beta}_1 \cos 2\pi f_0 t + \widehat{\beta}_2 \sin 2\pi f_0 t, \quad (1)$$

where $\widehat{L}$ is the regression estimate of LWP, t is time in days, and f_0 is the regression frequency, which is 1 cycle per day. Regression estimates of the amplitude and phase of the LWP diurnal cycle, denoted as $\widehat{A}_L$ and $\widehat{P}_L$, respectively, are computed from these regression parameters using $\widehat{A}_L = (\widehat{\beta}_1^2 + \widehat{\beta}_2^2)^{1/2}$ and $\widehat{P}_L = \tan^{-1}\frac{\widehat{\beta}_2}{\widehat{\beta}_1}$. Note that $\widehat{\beta}_0$ is very close to the time-mean LWP $\overline{L}$, although these two quantities are not formally identical owing to the independent methods of computing each.

2.3 Characterization of satellite sampling

The sampling frequency of the four-satellite combination varies significantly in space due to the swath width and mission orbital parameters of each satellite. It is thus of interest here to investigate the sampling errors of the diurnal cycle from this 4-satellite combination. A map of the total number of observations over the 42-day period 20 October–30 November 2008 during VOCALS-REx is shown in Fig. 1c. The total number of observations vary from about 250 along 30° S to about 170 along 10° S, which averages out to 6 and 4 observations per day, respectively, at each grid point over the ocean. The poleward increase in the number of observations is due to the poleward convergence of meridians, while the satellite swath has a fixed width. Of interest for this analysis is the sampling distribution throughout each day, which is shown by histograms of the observation time as functions of UTC Hour over the 42-day VOCALS-REx period (Fig. 1b) for the region shown in Fig. 1c. The SSM/I's and AMSR-E are polar-orbiting satellites having sun-synchronous orbits, which sample each grid cell at nearly the same local solar time each day. Observation times for each of these

ACPD
11, 31159–31206, 2011

satellites are clustered around two times per day corresponding to an ascending and descending ground track, with equatorial crossing times separated by close to 12 h. TMI observation times, on the other hand, are nearly uniformly distributed over the 42-day VOCALS-REx period (Fig. 1b) because of its low-inclination near-equatorial orbit, which was designed specifically to resolve diurnal variability over monthly timescales in the tropics and subtropics. It is this sampling pattern that Wood et al. (2002) exploited to estimate the LWP diurnal cycle equatorward of 40° latitude for the 2-yr period January 1999–December 2000.

Detailed spatial and temporal measurement distributions over the southeast Pacific for each satellite are illustrated in Fig. 2. Measurement locations along 5°, 20°, and 35° S are shown in time-longitude sections for an arbitrary 24-day period spanning the longitude range 80° to 100° W. Horizontal lines represent the times and locations of the measurements, with black lines corresponding to ascending swaths and red lines descending. As each satellite traverses through the region, the longitude of the swath steadily changes with latitude. These latitudinal variations produce repeated patterns of sampling bursts, where several measurements relatively close in time are followed by prolonged data gaps. A clear example of a sampling burst occurs with the SSM/I F13 along 20° S (Fig. 2b), where 6 consecutive measurements within about 3 days are followed by a data gap of nearly 4 days, and then subsequently repeated. Sampling bursts are particularly acute for the two SSM/I satellites, although the F13 sampling bursts tend to fall partially within the data gaps of the F15 and vice versa. Similar patterns of sampling bursts are apparent in all panels in Fig. 2. The TMI sampling pattern at 35° S shows very closely spaced measurements in time followed by nearly day-long data gaps (Fig. 2d); note that the TMI sampling bursts at this latitude make the ascending and descending swaths difficult to differentiate visually in this figure.

To demonstrate the latitudinally-varying spatial and temporal sampling that results from these sampling patterns, the revisit interval between consecutive LWP measurements Δt for the four-satellite combination is shown by the histogram in Fig. 3a. This two-dimensional histogram was computed as a function of latitude (y-axis) and Δt (x-

ACPD
11, 31159–31206, 2011

axis), and has the summation of all valid measurements between 240° and 292° W for the 4-yr period January 2005–December 2008. The revisit interval Δt is almost completely less than 6 h. Additionally, at higher latitudes, Δt has two separate clusters at about 2 and 4 h. Closer to the equator, the sampling interval is clustered around 4 h. The diurnal cycle is thus adequately sampled over the entire range of latitudes considered here from the four-satellite combination. Contrast this with the sampling pattern of just the TMI satellite, whose histogram of Δt is shown in Fig. 3b. Near the equator, Δt is nearly 12 h, while at higher latitudes, there is a bifurcation of Δt with alternating short and long data gaps caused by the uneven temporal sampling of the TMI satellite away from the equator, as apparent in Fig. 2d. There is also a significant fraction of measurements with Δt ~23 h over all latitudes. Lower-frequency variability, such as the seasonal cycle, can thus alias into the diurnal cycle estimated solely by TMI since it takes about a month to measure at every hour in the day. The improved sampling of the 3 additional satellites over TMI alone is clearly shown by the much smaller Δt over all latitudes.

To obtain estimates of the sampling errors of the diurnal cycle regression coefficients that can be expected from the four-satellite sampling and the analysis strategy employed here, synthetic diurnally-varying LWP time series are generated at 30-day intervals and then subsampled at the actual satellite observations times over the domain shown in Fig. 1c. The synthetic LWP time series were computed from

$$\widehat{L} = \beta_0 + \beta_1 \cos 2\pi f_0 t + \beta_2 \sin 2\pi f_0 t + \widehat{L}_{\text{rvar}}, \quad (2)$$

where f_0 is the diurnal frequency, t is the UTC time, and the coefficients β_0, β_1, and β_2 are specified as constant. Regression estimates of these coefficients, denoted as $\widehat{\beta}_0$, $\widehat{\beta}_1$, and $\widehat{\beta}_2$, are then obtained from the LWP synthetic time series subsampled at the actual satellite observation times at 30-day intervals to see how closely they match those used to construct the synthetic time series. The synthetic time series were constructed using $\beta_0 = 100\,\text{g m}^{-2}$, $\beta_1 = -35\,\text{g m}^{-2}$, and $\beta_2 = 7\,\text{g m}^{-2}$. This choice of coefficients gives a maximum LWP around sunrise and a realistic amplitude A_L =

ACPD
11, 31159–31206, 2011

35.7 g m^{-2} (red curve, Fig. 4a). To include an estimate of measurement uncertainty, uniformly-distributed random noise $\widehat{L}_{\mathrm{rvar}}$ was added to the synthetic time series to yield an RMS difference of 25 g m^{-2}.

An example 4-day section of the synthetic LWP time series $\widehat{L}$ computed in this manner is shown by the black curve in Fig. 4a. The points subsampled from this synthetic time series at the satellite observation times are shown in Fig. 4b, chosen arbitrarily at 85° W, 20° S. The diurnal regression estimate computed from the 30-day synthetic time series subsampled at the satellite observation times is shown by the green curve in Fig. 4b, which closely matches the noise-free synthetic time series shown by the red curve. At least qualitatively, the sampling and analysis strategy used here appears to accurately estimate diurnal variability.

To provide a more rigorous evaluation, this calculation was repeated for all grid points over the region shown in Fig. 1c and for all 30-day intervals during the period June 2002–May 2009. Histograms of the regression coefficient estimates relative to their "true" values, i.e., $\beta_0 - \widehat{\beta}_0$, $\beta_1 - \widehat{\beta}_1$, and $\beta_2 - \widehat{\beta}_2$, were computed from the four-satellite combination and are shown by the black curves in Fig. 5a–c. The histograms show that the regression coefficient differences are very nearly Gaussian distributed with zero mean, and hence are virtually unbiased in this example. The standard deviations of these histograms are between 2.2 and 3.2 g m^{-2} as listed in black in each panel. Histograms of the regression coefficient differences computed from just the TMI satellite have much broader Gaussian distributions, with standard deviations that are approximately double those obtained from the four-satellite combination. Histograms of the LWP diurnal cycle amplitude sampling errors, $A_L - \widehat{A}_L$, are nearly the same as those in the individual regression coefficients, with standard deviations of 3.0 g m^{-2} for the four satellite combination and 6.0 g m^{-2} for the TMI-only (Fig. 5d). Distributions of the phase sampling errors ($\frac{24}{2\pi}\left(\tan^{-1}(\widehat{\beta_2}/\widehat{\beta_1}) - \tan^{-1}(\beta_2/\beta_1)\right)$; Fig. 5e) have standard deviations of 0.3 h for the four-satellite combination and 0.7 h for the TMI-only. The uncertainty of the regression coefficients represented by the dynamic range of these histograms

ACPD
11, 31159–31206, 2011

result mostly from sampling errors in the presence of measurement uncertainty; if $\widehat{L}_{\text{rvar}}$ is set to zero, the standard deviations of the distributions are nearly zero (not shown).

Maps of the standard deviations of the regression coefficient difference estimates $\beta_0 - \widehat{\beta}_0$, $\beta_1 - \widehat{\beta}_1$, and $\beta_2 - \widehat{\beta}_2$ demonstrate the spatial distribution of the satellite sampling errors in this example (Fig. 6). These were computed as the standard deviation of the regression coefficient estimates from all 30-day sections in the analysis period. The standard deviations computed from the four-satellite combination, shown in the left column of panels, have a fairly uniform spatial distribution. In contrast, the TMI-only standard deviations have a roughly factor of 2 latitudinal variation and are largest near 40° S latitude, minimum along about 28° S, and increase closer to the equator. The large sampling errors near 40° S are a consequence of the sampling bursts of the TMI measurements, where alternating short and long revisit intervals at higher latitudes lead to large uncertainties of the LWP diurnal cycle.

This calculation yields an estimate of the sampling errors of the diurnal regression coefficients attributable to the complex spatial-temporal distribution of the satellite observations. The information provided by the additional 3 satellites used here significantly improves the expected sampling errors of the LWP diurnal cycle. Once natural temporal variability of the underlying diurnal cycle of LWP and synoptic weather variability are taken into account, the actual sampling errors in the diurnal cycle regression coefficient estimates will undoubtedly be significantly larger than the estimates provided by this simple example. However, this example provides some insight into the nature of the expected sampling errors since accurate and independent estimates of LWP on the time and space scales of the satellite observations are not available.

2.4 Comparison of collocated LWP between satellites

To assess the relative precision of the satellite LWP, the irregular temporal sampling of the TMI is exploited here to investigate collocated differences of LWP between the TMI and the other three satellites. TMI LWP measurements are collocated with those

ACPD
11, 31159–31206, 2011

from the other 3 satellites that occurred within ±20 min. The RMS and mean differences relative to TMI were computed at 3-month intervals over the geographical region shown by the rectangle in Fig. 7a. Time series of these statistics are shown in Fig. 7b and c, respectively. The black horizontal line in Fig. 7b represents the 25 g m^{-2} RMS uncertainty of the microwave LWP retrievals reported previously (Wentz, 1997; Wentz and Meissner, 2000). The RMS differences relative to TMI are mostly between 20 and 40 g m^{-2} and exhibit fairly little change over the 7-yr data record. Also apparent in this figure is a slight increase of roughly 10 g m^{-2} of the RMS differences during March-June of most years for all instruments. The source of this apparent pattern of the RMS differences is not known. AMSR-E consistently shows the smallest LWP RMS difference relative to TMI. Finally, as Fig. 7c shows, the LWP mean differences relative to TMI are between ±5 g m^{-2} for all instruments and years and do not exhibit any long-term trends. This analysis demonstrates that the combination of satellite instruments used here gives reasonably consistent estimates of LWP relative to each other. It is thus expected that errors in the diurnal cycle estimation associated with measurement and calibration differences between instruments are not likely significant.

3 7-yr mean LWP and LWP diurnal cycle

The regression variables $\widehat{\beta}_0$, $\widehat{A}_L$, and $\widehat{P}_L$ were computed for all consecutive 30-day periods during June 2002–May 2009 over the southeast Pacific using the four-satellite combination. Examples of the 7-yr mean LWP bin-averaged as a function of local solar time (LST) are shown in Fig. 8 for the squares marked in the accompanying map of the 7-yr mean $\widehat{\beta}_0$. LST varies as a function of longitude and matches UTC time at the prime meridian. The time-mean $\widehat{\beta}_0$ map shown here is related closely to the mean LWP field over the same period. The closeness of these two fields is evident from comparison of the map in Fig. 8 with the mean TMI LWP field shown in Fig. 7a. The individual points were chosen as examples of the various significant LWP features in the southeast Pacific. The gray points in the right column of panels in Fig. 8 represent the mean LWP

ACPD
11, 31159–31206, 2011

values for each hourly bin, and the error bars represent ±1 standard deviation about the mean, both computed for the 7-yr analysis period. Also shown by the dashed curves are the regression estimates of the LWP diurnal cycle. Figure 8 shows that the mean LWP diurnal cycle amplitude varies significantly within the southeast Pacific region and that the maximum LWP generally occurs in the early morning, consistent with previous studies. Additionally, the regression estimates of the LWP diurnal cycle, as illustrated by comparing the dashed curves to the gray points, capture the LWP diurnal cycle well for most locations.

Besides the diurnal cycle, a signficant semi-diurnal cycle in LWP is also evident in the hourly binned averages at 75° W, 18° S (Fig. 8c). This semi-diurnal cycle has also been observed previously over this region of the southeast Pacific from satellite LWP fields by O'Dell et al. (2008). The LWP semi-diurnal cycle is discussed further in Sect. 6.

Maps of the 7-yr means of the LWP diurnal cycle regression parameters are shown in Fig. 9 and are now discussed further.

3.1 Correlation coefficient

Correlation coefficients between the observed LWP L and the regression estimate $\widehat{L}$ obtained from Eq. (2) were computed pointwise for each 30-day interval during the 7-yr period June 2002–May 2009. The 7-yr time-mean correlation coefficient field is shown in Fig. 9a. The peak correlation coefficient of 0.58 is centered near 85° W, 20° S. Over the majority of the domain, the correlation coefficient is above 0.15. A locally minimum correlation is offshore and parallel to the Peruvian coastline where semi-diurnal LWP variability becomes significant (O'Dell et al., 2008, and as discussed in Sect. 6). Inshore of this minimum, the correlation coefficient reaches a local maximum of about 0.4. The correlation is below 0.2 in the SITCZ and the SPCZ. The southward decrease of the correlation coefficient is a consequence of the increased mid-latitude synoptic weather variability and proximity to the South Pacific Convergence Zone (SPCZ; e.g., Folland et al., 2002), which is oriented diagonal through the southwestern part of this analysis domain from the northwest to southeast. The correlation coefficient also

ACPD
11, 31159–31206, 2011

decreases close to the equator, where deep convective activity evidently accounts for more LWP variability than does the diurnal cycle.

3.2 Mean LWP $\widehat{\beta}_0$

The 7-yr mean $\widehat{\beta}_0$ is shown in Fig. 9b. It is minimum along the South American coast, particularly from southern Ecuador southward along Peru between 4° S and 17° S and along the southern Chilean coast between 25° S and 36° S in the outflow region of the Chilean low-level jet. In both regions, the mean $\widehat{\beta}_0$ is between 40 and 50 g m^{-2}. A local LWP maximum of about 100 g m^{-2} is centered near 85° W, 17° S and is associated with the main stratocumulus cloud deck over the subtropical southeast Pacific. The LWP increases toward the south, exceeding 120 g m^{-2} and is associated with interactions between extratropical synoptic weather variability and the southeast edge of the SPCZ. Along 5° S, there are slightly elevated values of LWP in this 7-yr mean, which are driven by low-level moisture convergence and convection in what is considered a distinct southern branch of the ITCZ, designated as the Southern ITCZ (SITCZ; e.g., Waliser and Gautier, 1993; Zhang, 2001; de Szoeke et al., 2006). While the SITCZ is not particularly prominent in the mean LWP fields, it is shown in Sect. 4 that temporal variability of the SITCZ is a significant coherent feature of the temporal LWP variability over the southeast Pacific. The SITCZ is generally distinct in the LWP field only in the boreal autumn, which can be seen, for instance, in Fig. 6b of O'Dell et al. (2008).

3.3 LWP diurnal cycle amplitude $\widehat{A}_L$

The 7-yr mean diurnal cycle amplitude $\widehat{A}_L$ is shown in Fig. 9b; these time-mean fields were computed from $\widehat{\beta}_1$ and $\widehat{\beta}_2$ at each 30-day interval using $\widehat{A}_L = \left(\widehat{\beta}_1^2 + \widehat{\beta}_2^2\right)^{1/2}$ and then scalar-averaged over the full 7 yr. The diurnal cycle amplitude largely mirrors the mean $\widehat{\beta}_0$ field shown in Fig. 9a, at least outside of the SPCZ. A maximum amplitude of ~40 g m^{-2} is located near the maximum in the mean LWP field near 85° W, 20° S. At this

ACPD
11, 31159–31206, 2011

location, the morning-to-afternoon LWP transition is thus ~80 g m^{-2}, which is a large fraction of the time-mean LWP here of ~100 g m^{-2}. In the early morning, the LWP is thus about 140 g m^{-2} on average, while in the late afternoon, it is about 60 g m^{-2}, which agrees with the binned scatterplot in Fig. 9d at this point. Parallel to the Peruvian coast, $\widehat{A}_L$ reaches a minimum of between 10 and 20 g m^{-2} about 200–300 km offshore, eventually joining the coast near southern Peru. This minimum is located slightly more offshore than the nearshore minimum in the time-mean $\widehat{\beta}_0$ shown in Fig. 7a. Besides this, there is a slight enhancement of the diurnal cycle amplitude within the SPCZ. A local minimum of $\widehat{A}_L$ is located near 75° W, 35° S, which is a region noted for the location of the Chilean low-level jet (CLLJ). North of here in the CLLJ outflow region, $\widehat{A}_L$ increases substantially in a thin ribbon that starts along the central Chilean coastline and extends westward to join with the main southeast Pacific stratiform cloud deck. Finally, within the SITCZ along ~5° S, there is little diurnal variability in the LWP field. The amplitudes of the LWP diurnal cycle over the southeast Pacific found here are broadly consistent with those found in Zuidema and Hartmann (1995), Wood et al. (2002), and O'Dell et al. (2008).

The fraction of the mean LWP accounted for by the diurnal cycle is shown quantitatively by computing the 7-yr mean $\widehat{A}_L$ normalized by the 7-yr mean $\widehat{\beta}_0$ (Fig. 10a). The normalized diurnal amplitude is about 0.4 over much of the domain. Within about 200 km of the South American coast, the normalized amplitude increases above 0.6. Offshore of this maximum along the Peruvian coast, there is a notable localized minimum of about 0.2. Approaching the SPCZ, the normalized minimum approaches 0.2. These values are generally similar to the 2-yr mean normalized amplitudes in Fig. 3 of Wood et al. (2002). The normalized amplitudes are generally much stronger in November (Fig. 10b) than during April (Fig. 10c). As shown in more detail in the next section, the diurnal cycle amplitude reaches its temporal extremum around November over the southeast Pacific. This apparent seasonality agrees qualitatively with the seasonality observed in Fig. 10 of O'Dell et al. (2008), although July and January were shown in that study.

ACPD
11, 31159–31206, 2011

3.4 LWP diurnal cycle phase $\widehat{P}_L$

The local solar time of the diurnal maximum LWP is shown in Fig. 9d. Consistent with previous satellite-based studies (e.g., Fig. 3 in Wood et al. 2002 and Fig. 10 in O'Dell et al. 2008), the LWP over the southeast Pacific is maximum during the early morning hours and minimum during the late afternoon. The spatial structure of the LWP diurnal phase is quite different from the mean amplitude and $\widehat{\beta}_0$. Within a thin strip extending roughly ∼300 km offshore of the Peruvian coastline, the LWP diurnal cycle peaks at around 06:00 LST. A similar strip exists adjacent to the central Chilean coastline, but extends further offshore. Between these two strips centered on the Arican Bight near the northern Chilean coast, the diurnal cycle peaks earlier at about 02:00 LST. In the region containing the maximum in the diurnal cycle amplitude centered near 85° W, 20° S, the diurnal cycle peaks at about 03:00 LST. Progressing westward from here, the local maximum occurs later in the morning, although diurnal variability is less prominent in these regions (Fig. 9a and c).

4 Seasonal and interannual variability of LWP diurnal regression coefficients

Spatio-temporal variability of the scalar $\widehat{\beta}_0$ and the diurnal cycle amplitude $\widehat{A}_L$ fields on seasonal and longer timescales is investigated here using conventional empirical orthogonal function (EOF) analysis. The EOFs were computed from the regression estimates of $\widehat{\beta}_0$ and $\widehat{A}_L$ at 30-day intervals for the 7-yr period June 2002–May 2009 for the southeast Pacific region between 69° W and 115° W and between the equator and 39° S. As is customary, the EOFs were computed after removing the 7-yr mean fields shown in Fig. 9. The EOFs for $\widehat{\beta}_0$ are shown in Fig. 11 and those for $\widehat{A}_L$ are shown in Fig. 12. The amplitude time series are shown in the left column of panels and the spatial modes, which have been normalized to unit interval, are shown in the right column of panels.

ACPD
11, 31159–31206, 2011

4.1 Mean LWP $\widehat{\beta}_0$

The first four dominant EOF modes of $\widehat{\beta}_0$ are shown in Fig. 11. The dominant mode of variability of $\widehat{\beta}_0$, accounting for 32.9 % of the total LWP variance, describes a regular annual cycle involving the SITCZ and much of the cloud field in the eastern half of the domain. A relatively sharp peak occurs in the austral autumn between March and April, while a broader minimum occurs during the austral spring between August and October. The peak-to-trough magnitude of the first mode is about $80\,\mathrm{g\,m^{-2}}$; its minimum is about $-30\,\mathrm{g\,m^{-2}}$ and maximum is about $50\,\mathrm{g\,m^{-2}}$. The spatial pattern of this mode shows largest positive values in a zonal band centered on the SITCZ and terminating just east of the Galapagos islands. The maximum LWP associated with the SITCZ is thus maximum during austral autumn, which is consistent with previous observations of the annual cycle of the SITCZ (e.g., Waliser and Gautier, 1993; Zhang, 2001; O'Dell et al., 2008). Significant positive values also occur within the Gulf of Guayoquil near the Peru-Ecuador border. Strong variability of the opposite sign occurs to the south and east of the SITCZ, which is marked by the largest negative values of this spatial mode in the southeast Pacific. A broad zonal band of negative spatial mode centered near 13° S extends westward throughout most of the analysis domain. There are also much weaker coherent variations of the same sign off the central coast of Chile and of opposite sign along the SPCZ; the numerical values of the spatial mode in these regions indicate that these variations are much weaker in magnitude than those encountered within the SITCZ by more than 50–90 %. Finally, we note that there are some interannual variations in this first-mode EOF, particularly during the austral autumn of 2009, where the $\widehat{\beta}_0$ first-mode amplitude time series reaches a peak of $70\,\mathrm{g\,m^{-2}}$.

The second mode EOF of $\widehat{\beta}_0$ accounts for 15.1 % of the total LWP variance and describes variability mostly along the SITCZ (Fig. 11). The amplitude time series shows that the maximum $\widehat{\beta}_0$ associated with this mode of variability occurs mainly in the austral spring, between September and November, and minima shifted by about 6 months.

ACPD
11, 31159–31206, 2011

This annual cycle is interruputed several times by large amplitude transitions in $\widehat{\beta}_0$ during austral autumn, however, with about 100–160 g m^{-2} changes in $\widehat{\beta}_0$ occurring in adjacent 30-day data blocks. Within the 7-yr data record analyzed here, the most prominent of these transitions occur between March and April of the years 2004, 2006, and 2009. Similar but much smaller transitions can be seen during the same months in most other years. Localized minima also occur between June and July of every year, with some years stronger than others. For instance, the minima in June 2005 is much weaker than during all other years. The peak-to-trough amplitude of the annual cycle described by this mode is roughly ±20 g m^{-2}.

The third mode EOF of $\widehat{\beta}_0$ accounts for 12.4 % of the total LWP variance and describes annual variability mainly within the SPCZ and SITCZ. A sharp peak of the $\widehat{\beta}_0$ associated with this mode occurs during the late austral autumn between April and June. Variations from peak-to-trough are between about ±35 g m^{-2}. The map of the spatial mode indicates that this mode of variability is large and positive over the SPCZ and large and negative to the east of the Galapagos islands. The negative values of the spatial mode follow the coast southward to about the coastal city of Pisco, Peru. Smaller positive values of the spatial mode occur within the SITCZ. Between the SITCZ and the SPCZ, a local minimum of the spatial mode is centered at about 100° W, 15° S.

The fourth mode EOF of $\widehat{\beta}_0$ accounts for 6.1 % of the total LWP variance. Its amplitude time series shows irregular temporal variability. The spatial mode shows maximum positive values east of the Galapagos and negative values across a broad arc of the southeast Pacific starting along the central Chilean coastline near 25° S and extending thousands of kilometers northwest. Along the northern edge of this arc is a sharp contrast between negative and positive values of the spatial mode. This mode is suggestive of variability in coherent large-scale circulation patterns.

ACPD
11, 31159–31206, 2011

4.2 LWP diurnal cycle amplitude $\widehat{A}_L$

The first two EOFs of the diurnal cycle amplitude contain annual cycles of differing phases and spatial signatures, as shown in Fig. 12. The first EOF of $\widehat{A}_L$ accounts for 23.5 % of the total variance of $\widehat{A}_L$ and describes an annual cycle with sharp peaks in the austral summer between November and December and troughs during the austral winter. The peak-to-trough amplitude of the seasonal cycle is about 40 g m^{-2} and has a maximum slightly higher than the minimum. Aside from comparatively smaller peaks near the end of 2004 and 2005, no significant interannual variability is evident in the first mode EOF of $\widehat{A}_L$. Collectively, the spatial pattern of this mode is similar to the 7-yr mean $\widehat{A}_L$ fields shown in Fig. 9b. The spatial mode is mostly positive throughout the whole domain and has a maximum located near 85° W, 20° S. The significant positive values of the spatial mode throughout most of the domain indicates that the variability associated with this mode represents a coherent in-phase seasonal cycle throughout the southeast Pacific which peaks during the austral summer.

The second EOF of $\widehat{A}_L$ captures 10.7 % of the total variance and also features a prominent annual cycle, although the peak is during March of each year and the minimum is between September and October (Fig. 12). The amplitude of the annual cycle of $\widehat{A}_L$ associated with this mode is about 30 g m^{-2}. This EOF mode of $\widehat{A}_L$ bears a strong resemblance to the first EOF mode of $\widehat{\beta}_0$ shown in Fig. 11 in both the amplitude time series and the pattern of the spatial mode. The amplitude of the LWP diurnal cycle is thus linked to the time-mean LWP, with stronger diurnal variations in regions with higher mean LWP. The spatial mode also shows a broad band of negative amplitudes near the Peruvian coast between ~8° and 18° S which attains a maximum absolute magnitude at the coastline and decaying westward. In this latitudinal band, the $\widehat{A}_L$ thus peaks during the austral spring and reaches a minimum during the austral autumn, opposite to what occurs to the south where the EOF spatial mode is positive.

The third and fourth modes of the $\widehat{A}_L$ EOFs account for 4.6 % and 3.2 % of the total variance in $\widehat{A}_L$, respectively. The amplitude time series of both are highly intermittent

ACPD
11, 31159–31206, 2011

and punctuated by several sharp transitions between consecutive 30-day periods. The spatial structure of the third mode EOF shows a band of variability associated with the SITCZ, although it appears noisy and irregular. The spatial structure of the fourth mode does not appear to represent any significant features in the $\widehat{A}_L$ field.

4.3 LWP diurnal cycle phase

Coherent spatial and temporal variability of the diurnal cycle phase is much more difficult to determine due to 360-degree discontinuities of the phase angle which occur within the analysis domain. Time-longitude plots of the diurnal cycle phase angle are shown in Fig. 13a along 20° S and in Fig. 13b along 15° S. Along 20° S, there is evidence of a seasonal cycle in the phase east of 90°E extending to the South American coast; within this longitude range, maxima in the LWP diurnal cycle occur around midnight LST during the austral winter and 03:00 LST during the austral summer. West of 100° W, the amplitude of the diurnal cycle is below 20 g m^{-2} and the phase becomes much noisier.

5 LWP diurnal cycle regression comparisons for 20 October–30 November 2002–2008

LWP variability during the same time period as VOCALS-REx is now analyzed to compare conditions during the experiment with those experienced during other years. The diurnal cycle is computed as before, except for the 42-day period 20 October–30 November during the 7 yr between 2002 and 2008.

5.1 Time-mean diurnal cycle

A map of $\widehat{\beta}_0$ averaged for 20 October–30 November 2002–2008 (Fig. 16b) shows regions with markedly different LWP. The mean LWP is minimum along the Peruvian

ACPD
11, 31159–31206, 2011

coastline between about 12° S and 17° S latitude and extending roughly 500 km seaward. Low LWP values extend southward to about 25° S, which corresponds roughly to the outflow of the CLLJ. In this region, the mean LWP increases abruptly from about 50 g m^{-2} to about 90 g m^{-2}, starts along the coast at about 27° S, and extends northwestward in a banded structure that widens as it merges with the main stratocumulus deck. In this banded structure, the mean LWP increases from about 90 g m^{-2} at 27° S, weakens slightly towards the northwest, then increases to a maximum of 120 g m^{-2} at about 83° W, 18° S. The areal extent of the main stratocumulus deck broadens considerably west of 80° W. In the core of the CLLJ south of 75° W, 25° S, the mean LWP decreases to below 50 g m^{-2}. South of 30° S, LWP variability during the VOCALS-REx period is dominated by mid-latitude synoptic variability rather than by diurnal variability.

The mean $\widehat{A}_L$ during 20 October–30 November 2002–2008 (Fig. 16c) has a comparable spatial structure to the $\widehat{\beta}_0$ fields shown in Fig. 16b. Minimum values of between 10 and 15 g m^{-2} are found along the Peruvian coast and near the CLLJ at 75° W, 30° S. In the banded structure north of the CLLJ, the amplitude increases sharply to between about 40 and 50 g m^{-2}. The maximum amplitudes are shifted about 500 km southeast of the maximum $\widehat{\beta}_0$, with values of about 65 g m^{-2} at 82° W, 21° S. In most parts of the domain, the mean $\widehat{A}_L$ during 20 October–30-November is more than half of the mean LWP, as can be seen by comparing the normalized amplitude during November 2002–2008 shown in Fig. 10c with the complete 7-yr period shown in Fig. 10a.

The time-averaged correlation coefficients between the diurnal regression and the raw observations (Fig. 16a; or equivalently, the square root of the regression model skill) is quite similar in spatial structure to the amplitude of the diurnal regression coefficients shown in Fig. 16c. They are also generally greater than the correlation coefficients for the complete 7-yr period shown in Fig. 10a. The maximum correlations of about 0.65 are centered over the main stratocumulus cloud deck in the central portion of the domain centered over 20° S, 85° W. On average, the diurnal cycle thus explains approximately 40 % of the LWP variance in these regions. Along the Peruvian coastline and the southern portions of the domain, the correlations are between 0.15 and 0.2.

ACPD
11, 31159–31206, 2011

The phase of the LWP diurnal cycle is shown in Fig. 16d in terms of local hour of maximum LWP. Over the whole domain, the maximum diurnal cycle occurs between 00:00 and 08:00 LST. From the Peruvian coastline to about 18° S, the peak LWP occurs between about 05:00 LST and 08:00 LST. Between 18° S and 25° S, peak LWP occurs earlier, between 00:00 LST and 02:00 LST. Going westward along this latitudinal range, the peak LWP occurs slightly later at around 03:00 LST. Finally, there is a region south of 25° S and east of 75° W that has a much later peak time of LWP. Close to the South American coast, LWP variability is also significantly influenced by a semi-diurnal cycle in addition to the diurnal cycle, as discussed in Sect. 6.

5.2 Intraseasonal variability of the LWP diurnal cycle

Maps of $\widehat{\beta}_0$ anomalies for 20 October–30 November for each year between 2002 and 2008 are shown in Fig. 17. Generally, the $\widehat{\beta}_0$ anomalies are between $\pm 25\,\mathrm{g\,m^{-2}}$. Probably the most anomalous year is 2006, where the whole area to the north of about 20° S and east of 75° W have large negative LWP anomalies between -10 to $-20\,\mathrm{g\,m^{-2}}$. This year also has a remarkably smaller than average diurnal cycle amplitude in roughly the same area (Fig. 18), with amplitude anomalies of about -10 to $-20\,\mathrm{g\,m^{-2}}$ being about 15–35 % of the mean diurnal cycle amplitude. It is noteworthy that the area north of the CLLJ also contains smaller values of $\widehat{\beta}_0$ during 2006. Contrast 2006 with 2007, where the $\widehat{\beta}_0$ anomalies are positive over most of the domain away from the South American coastline, and are slightly negative near the northern Chilean coast. During 2008 and VOCALS-REx, the mean LWP is about $20\,\mathrm{g\,m^{-2}}$ greater than average in the CLLJ region and along the southern Peruvian coastline, and mostly average or slightly less than average elsewhere. The other main anomalous year was 2004, where south of 25° S had smaller than average LWP.

Besides 2006, anomalies of the diurnal cycle amplitude do not appear to be as well correlated with the $\widehat{\beta}_0$ anomalies (Fig. 18). In 2008, there are fairly strong positive anomalies emanating from the Chilean coast at about 27° S towards the northwest.

ACPD
11, 31159–31206, 2011

There is also a broad but patchy area of negative amplitude anomalies over the subtropical high centered near 84° W, 25° S. In 2005, there is a band of negative amplitude anomalies roughly parallel to and a few hundred kms offshore of the Peruvian coastline, and broadening out toward the northern portion of the domain.

Anomalies of the diurnal cycle phase were computed from $\frac{24}{2\pi}\tan^{-1}\left(\frac{<\widehat{\beta}_2>-\widehat{\beta}_2}{<\widehat{\beta}_1>-\widehat{\beta}_1}\right)$. Maps of the anomalous diurnal phase thus computed (Fig. 19) show strong interannual variability parallel to and offshore of the Peruvian coastline where a diurnal subsidence wave significantly influences the clouds and boundary layer structure (e.g., Garreaud and Muñoz, 2004). The difference in phase is about ±2 h. Also of note is 2007, where the hour of maximum in the diurnal cycle shifts to more than 1 h earlier in the morning, on average, over wide portions of the central and northern parts of the domain. A similar shift occurs in 2008 south of 25° S; the diurnal cycle amplitudes here, however, are not large compared to the mean $\widehat{\beta}_0$.

6 LWP semi-diurnal cycle

The LWP diurnal cycle regression analysis from Sect. 3 was repeated for the semi-diurnal frequency for the 7-yr analysis period. The amplitude and phase of the resulting LWP semi-diurnal cycle are shown in Fig. 14a and b, respectively. The LWP semi-diurnal amplitude (Fig. 14a) is largest along a strip roughly 300 km off the coast of Peru and northern Chile; this strip is closer to the coast near Ecuador and northern Peru. Within this strip, the LWP semi-diurnal cycle amplitude is between 15 and 20 g m^{-2}, with the 20 g m^{-2} maximum located near 75° W, 18° S. The LWP semi-diurnal cycle is thus a considerable fraction of the LWP diurnal cycle along this strip. Over the rest of the southeast Pacific, the LWP semi-diurnal cycle is of small amplitude. The location and magnitude of the semi-diurnal LWP amplitude shown here over the southeast Pacific are consistent with the April and October averages shown in Fig. 11 of O'Dell et al. (2008).

ACPD
11, 31159–31206, 2011

A map of the 7-yr mean phase of the LWP semi-diurnal cycle is shown in Fig. 14b. This map shows the hour of the first maximum of the semi-diurnal cycle during the morning hours (note that the second maximum is 12 h later than the first). The morning peak of the LWP semi-diurnal cycle is around 06:00 LST along the South American coast and occurs progressively later outward from the coast to roughly 11:00 LST. This westward phase transition is most apparent within the strip of elevated LWP semi-diurnal cycle amplitude shown in Fig. 14a.

The first four dominant EOFs of the LWP semi-diurnal amplitude are shown in Fig. 15. The most dominant mode accounts for 6.9 % of the variance. It describes an annual cycle that peaks during the austral spring time, about 3 months ahead of the peak in the first-mode EOF of the LWP diurnal cycle amplitude shown in Fig. 12. The peak-to-trough differences in this annual cycle are between about 15 and 20 g m^{-2}. Differences between austral spring and autumn shown by this EOF are consistent with the differences between the LWP semi-diurnal cycle amplitude between April and October shown by O'Dell et al. (2008). The spatial pattern of the first-mode EOF is largest within roughly 800 km of the Peruvian and northern Chilean coastline, with the maxima located off northern Peru. This maximum is roughly along the same strip as the maximum LWP semi-diurnal cycle amplitude shown in Fig. 14a.

The second and third EOFs of the LWP semi-diurnal cycle amplitude are fairly nondescript, although the amplitude time series of both show minor trends over the 7-yr data record. The fourth EOF, however, shows considerable seasonal variability in phase with the second-mode EOF of the LWP diurnal cycle as shown in Fig. 12. We note that the differences of variance between the presented modes (particularly between the first three) are not large and may not pass a significance test such as that proposed by North et al. (1982). However, statistical significance is difficult to evaluate since significant semi-diurnal variability appears to occupy only a small portion of the analysis domain near the coast; the large part of the domain without significant semi-diurnal variability dilutes the total variance explained by any particular EOF mode. Either a much larger time record or an analysis domain focused within 1000 km of Peru

ACPD
11, 31159–31206, 2011

are needed to characterize the variability in a statistically significant way. Nonetheless, we believe the first-mode EOF shown in Fig. 15 strongly suggests significant seasonal variability of the LWP semi-diurnal cycle.

7 Conclusions

Spatio-temporal variability of liquid water path (LWP) over the southeast Pacific Ocean was described using LWP observations from four satellite microwave radiometers (AMSR-E, TMI, SSM/I F13, and SSM/I F15) for the period June 2002–May 2009, corresponding to a complete 7 data record in which all four satellites were operational. This study quantifies seasonal and interannual variability of the LWP mean and diurnal cycle at 30-day intervals during the 7-yr analysis period using empirical orthogonal function analysis. While previous studies have mostly focused on the global ocean, this analysis focuses on LWP variability exclusively in the southeast Pacific, which allows a more complete and in-depth characterization of LWP variability in this region. This study was motivated in part by the VOCALS-REx program, which highlighted a need for observations of the cloud field in the southeast Pacific on the long time scales and large spatial scales provided by satellite observations.

The satellite observations show that the LWP field varies considerably in time and space within the southeast Pacific. The time-mean LWP is largest within the Southeast Pacific Convergence Zone (SPCZ). Of particular interest is the local LWP maximum of about 110 $\mathrm{g\,m^{-2}}$ located just north of 85° W, 20° S, which is embedded within the main stratiform cloud deck of the southeast Pacific. The time-mean LWP is a minimum along most of the South American coastline before increasing several hundred kilometers offshore. The nearshore minimum of LWP is more apparent in the region associated with the Chilean low-level jet (CLLJ) region along the southern coast of Chile. Enhanced LWP is also associated with the southern branch of the Intertropical Convergence Zone (SITCZ) in a zonal strip along 5° S.

ACPD
11, 31159–31206, 2011

EOF analysis indicates that the principal mode of variability of the LWP field is associated with increased activity in the SITCZ during boreal autumn. During the active phase of the SITCZ, coherent variations in LWP include decreased LWP along the Ecuadorian and Peruvian coastlines which extends westward to about 110° W, and increased LWP along the southern Chilean coast in the outflow region of the CLLJ. The second EOF involves a second but smaller active period of the SITCZ which occurs during the boreal spring; unlike the first mode, this mode of variability is just localized to the SITCZ.

Consistent with previous studies, diurnal variability of LWP is an $O(1)$ source of variability in the extensive stratiform cloud deck over the southeast Pacific. The time-mean diurnal cycle amplitude is more than 40 % of the total time-mean LWP over most of the southeast Pacific, reaching an amplitude of 40 g m^{-2} near 85° W, 20° S. In general, the mean LWP diurnal cycle amplitude bears a close resemblance to the time-mean LWP field such that the amplitude is largest where the highest mean LWP values occur. EOF analysis of the diurnal cycle amplitude shows strong seasonal variability throughout the southeast Pacific that has not been fully described before. For instance, the principal EOF of the diurnal cycle amplitude describes an annual mode that is typically largest during November and smallest during June–August, with peak-to-trough differences exceeding the time-mean diurnal cycle amplitude for most years. A second significant mode of variability also features an annual cycle with largest diurnal cycle amplitude during boreal autumn south of 20° S and during boreal spring from a latitudinal band between 10° S and 20° S.

These observations can be used to test the temporal and spatial LWP variability in numerical weather prediction and climate models, and to provide large-scale context to in situ obervations.

Acknowledgements. This work was performed while the lead author held a National Research Council Research Associateship Award at the Naval Research Laboratory, Monterey, California. This work was supported by the Office of Naval Research (ONR) under Program Element 0602435N and by the National Science Foundation (ATM-0749011).

ACPD
11, 31159–31206, 2011

References

Bergman, J. W. and Salby, M. L.: The role of cloud diurnal variations in the time-mean energy budget, J. Climate, 10, 1114–1124, 1997. 31162

Bretherton, C. S., Klinker, E., Betts, A. K., and Coakley, J.: Comparison of ceilometer, satellite, and synoptic measurements of boundary layer cloudiness and the ECMWF diagnostic cloud parameterization scheme during ASTEX, J. Atmos. Sci., 52, 2736–2751, 1995. 31162

de Szoeke, S. P., Wang, Y., Xie, S.-P., and Miyama, T.: Effect of shallow cumulus convection on the eastern Pacific climate in a coupled model, Geophys. Res. Lett., 33, L17713, doi:10.1029/2006GL026715, 2006. 31161, 31173

de Szoeke, S. P., Fairall, C. W., Wolfe, D. E., Bariteau, L., and Zuidema, P.: Surface flux observations on the southeastern tropical Pacific Ocean and attribution of SST errors in coupled ocean-atmosphere models, J. Climate, 23, 4152–4174, 2010. 31161

Folland, C. K., Renwick, J. A., Salinger, M. J., and Mullan, A. B.: Relative influences of the interdecadal Pacific Oscillation on the South Pacific Convergence Zone, Geophys. Res. Lett., 29, 1643, doi:10.1029/2001GL014201, 2002. 31172

Garreaud, R. D. and Muñoz, R.: The diurnal cycle in circulation and cloudiness over the subtropical southeast Pacific: A modeling study, J. Climate, 17, 1699–1710, 2004. 31162, 31182

Hannay, C., Williamson, D., Hack, J., Kiehl, J., Olson, J., Klein, S., Bretherton, C., and Köhler, M.: Evaluation of forecasted southeast Pacific stratocumulus in the NCAR, GFDL, and ECMWF models, J. Climate, 22, 2871–2889, 2009. 31161

Klein, S. A. and Hartmann, D. L.: The seasonal cycle of low stratiform clouds, J. Climate, 6, 1587–1606, 1993. 31161

Liu, G. and Curry, J. A.: Determination of characteristic features of cloud liquid water from satellite microwave measurements, J. Geophys. Res., 98, 5069–5092, 1993. 31165

Ma, C.-C., Mechoso, C. R., Robertson, A. W., and Arakawa, A.: Peruvian stratus clouds and the tropical Pacific circulation: A coupled ocean-atmosphere GCM study, J. Climate, 9, 1635–1645, 1996. 31161

Mechoso, C. R., Robertson, A. W., Barth, N., Davey, M. K., Delecluse, P., Gent, P. R., Ineson, S., Kirtman, B., Latif, M., Treut, H. L., Nahai, T., Neelin, J. D., Philander, S. G. H., Polcher, J., Schopf, P. S., Stockdale, T., Suarez, M. J., Terray, L., Thual, O., and Tribbia, J. J.: The seasonal cycle over the tropical Pacific in coupled ocean–atmosphere general circulation models, Mon. Weather Rev., 123, 2825–2838, 1995. 31161

Minnis, P. and Harrison, E. F.: Diurnal variability of regional cloud and clear-sky radiative param-

ACPD

11, 31159–31206, 2011

eters derived from GOES data: Part II: November 1978 cloud distributions, J. Appl. Meteor., 23, 1012–1031, 1984. 31162
Minnis, P., Heck, P. W., Young, D. F., and Snider, C. W. F. J. B.: Stratocumulus cloud properties derived from simultaneous satellite and island-based instrumentation during FIRE, J. Appl. Meteor., 31, 317–339, 1984. 31162
North, G. R., Bell, T. L., Cahalan, R. F., and Moeng, F. J.: Sampling errors in the estimation of empirical orthogonal functions, Mon. Weather Rev., 110, 699–706, 1982. 31183
O'Dell, C. W., Wentz, F. J., and Bennartz, R.: Cloud liquid water path from satellite-based passive microwave observations: A new climatology over the Global Oceans, J. Climate, 21, 1721–1739, 2008. 31162, 31165, 31172, 31173, 31174, 31175, 31176, 31182, 31183
Rozendaal, M. A., Leovy, C. B., and Klein, S. A.: An observational study of diurnal variations of marine stratiform cloud, J. Climate, 8, 1795–1809, 1995. 31162
Waliser, D. E. and Gautier, C.: A satellite-derived climatology of the ITCZ, J. Climate, 6, 2162–2174, 1993. 31173, 31176
Wang, S., O'Neill, L. W., Jiang, Q., de Szoeke, S. P., Hong, X., Jin, H., Thompson, W. T., and Zheng, X.: A regional real-time forecast of marine boundary layers during VOCALS-REx, Atmos. Chem. Phys., 11, 421–437, doi:10.5194/acp-11-421-2011, 2011. 31161
Wentz, F. J.: A well calibrated ocean algorithm for Special Sensor Microwave/Imager, J. Geophys. Res., 102, 8703–8718, 1997. 31171
Wentz, F. J. and Meissner, T.: AMSR Ocean Algorithm, Version 2, Tech. Rep. 121599A–1, Remote Sensing Systems, Santa Rosa, CA, available at: http://www.remss.com/papers/AMSR_Ocean_Algorithm_Version_2.pdf, 2000. 31171
Wood, R., Bretherton, C. S., and Hartmann, D. L.: Diurnal cycle of liquid water path over the subtropical and tropical oceans, Geophys. Res. Lett., 29, 2092, doi:10.1029/2002GL015371, 2002. 31162, 31167, 31174, 31175
Wyant, M. C., Wood, R., Bretherton, C. S., Mechoso, C. R., Bacmeister, J., Balmaseda, M. A., Barrett, B., Codron, F., Earnshaw, P., Fast, J., Hannay, C., Kaiser, J. W., Kitagawa, H., Klein, S. A., Köhler, M., Manganello, J., Pan, H.-L., Sun, F., Wang, S., and Wang, Y.: The PreVOCA experiment: modeling the lower troposphere in the Southeast Pacific, Atmos. Chem. Phys., 10, 4757–4774, doi:10.5194/acp-10-4757-2010, 2010. 31161
Zhang, C.: Double ITCZ, J. Geophys. Res., 106, 11785–11792, 2001. 31173, 31176
Zuidema, P. and Hartmann, D. L.: Satellite determination of stratus cloud microphysical properties, J. Climate, 8, 1638–1656, 1995. 31162, 31174

ACPD
11, 31159–31206, 2011

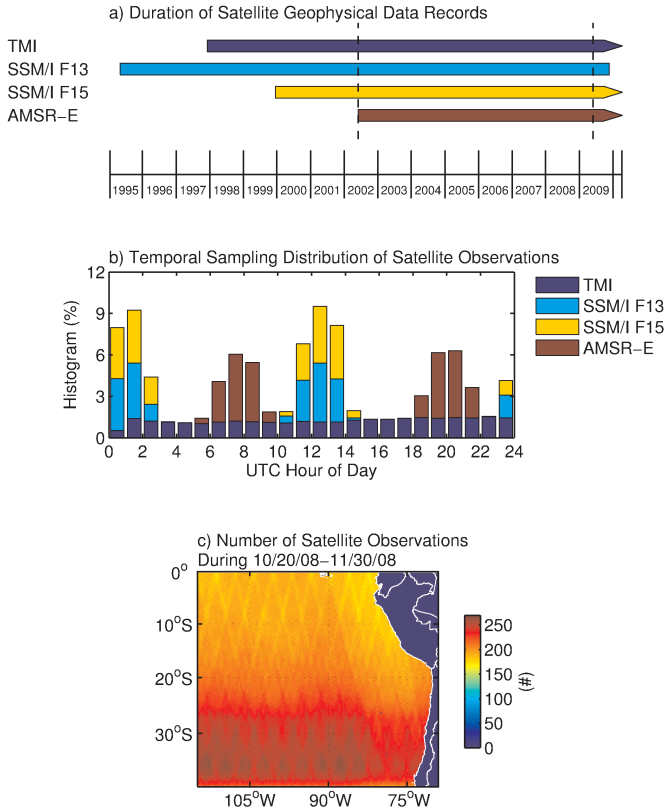

Fig. 1. **(a)** Timeline of the geophysical data records for each of the four microwave satellites used in this analysis. **(b)** Stacked bar chart of the temporal sampling distribution as a function of UTC Hour during the 42-day period 20 October 2008–30 November 2008 for the region shown in the map in **(c)**. **(c)** Map of the total number of gridded satellite observations in each 0.25° latitude by 0.25° longitude grid cell from the 4-satellite combination during the 42-day period 20 October 2008-30 November 2008.

ACPD
11, 31159–31206, 2011

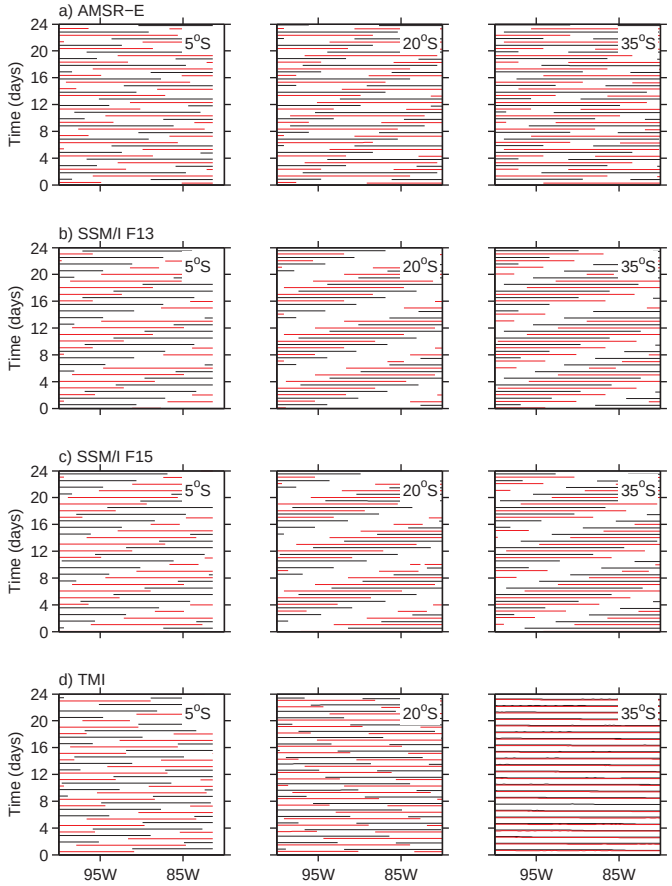

Fig. 2. Measurement locations at 5° S, 20° S, and 35° S, plotted in a time-longitude section for each of the satellites used in this analysis: **(a)** AMSR-E; **(b)** SSM/I F13; **(c)** SSM/I F15; and **(d)** TMI. Black lines represent ascending passes and red lines descending. The 24-day period shown here was arbitrarily chosen to start on 1 October 2008.

ACPD
11, 31159–31206, 2011

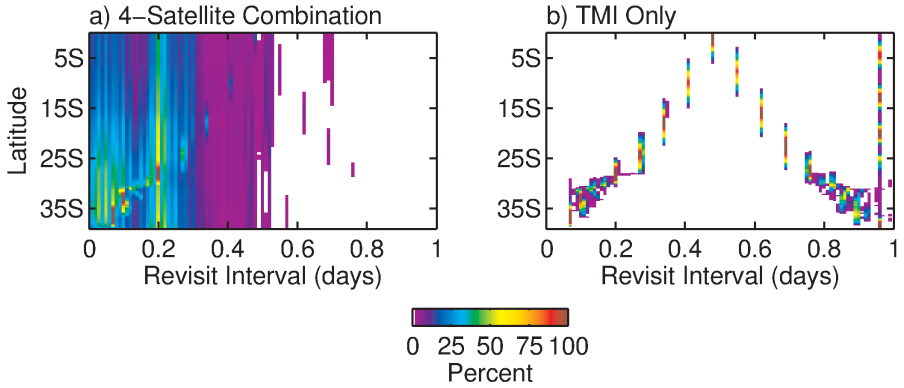

Fig. 3. Histograms of the revisit interval Δt (x-axis) as a function of latitude (y-axis) for **(a)** the 4-satellite combination (AMSR-E, TMI, and SSM/I F13 and F15) and **(b)** TMI only. The histograms were computed for each grid point and summed for all over-ocean grid points along each latitude between 240°–292° W over the 7-yr period June 2002–May 2009. Time-latitude bins with no observations are displayed as white.

ACPD
11, 31159–31206, 2011

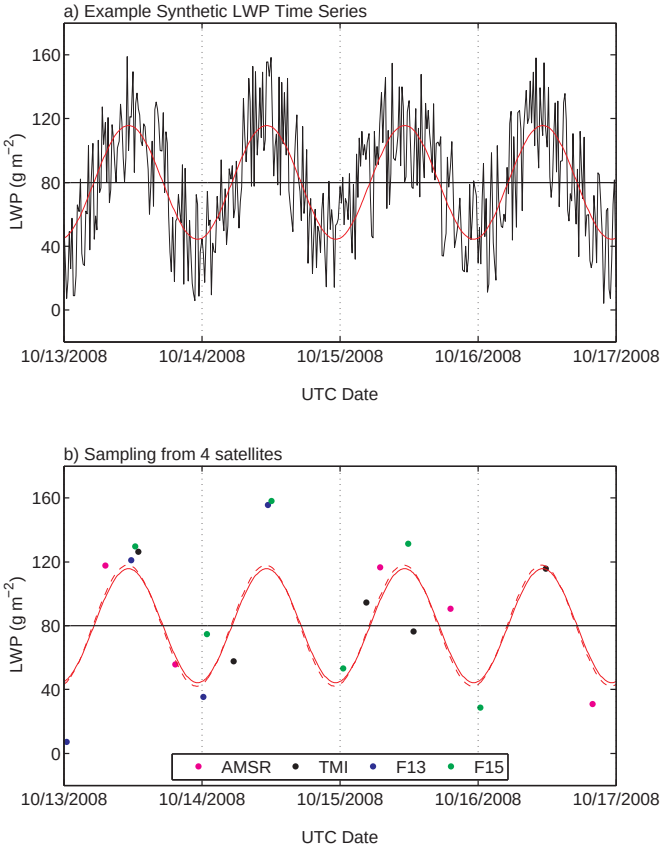

Fig. 4. (a) Example of a 4-day section of the LWP synthetic time series (black) and the noise-free LWP diurnal cycle (red). **(b)** The synthetic time series shown in **(a)** subsampled at the actual satellite observation times at 20° S, 85° W for the dates listed. The colors denote the individual satellites according to the legend at the bottom of the plot. The dashed red curve shows the least-squares fit of the points to sinusoids at the diurnal frequency.

ACPD
11, 31159–31206, 2011

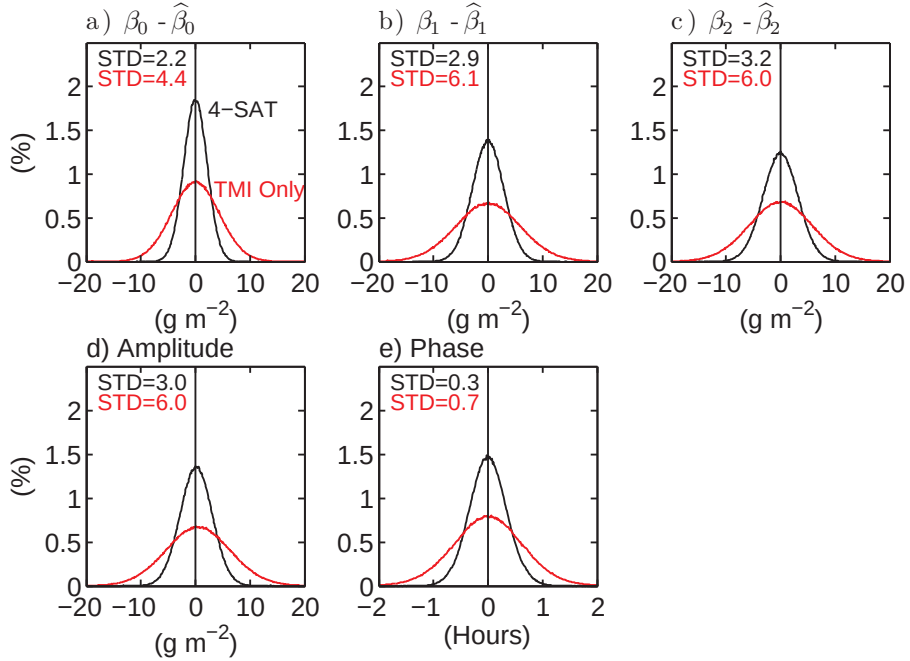

Fig. 5. Histograms of the sampling errors in the regression coefficients from the 4-satellite combination (black curves) and TMI only (red curves): **(a)** $\beta_0 - \widehat{\beta}_0$; **(b)** $\beta_1 - \widehat{\beta}_1$; **(c)** $\beta_2 - \widehat{\beta}_2$; amplitude $A_L - \widehat{A}_L$; and **(e)** phase $P_L - \widehat{P}_L$.

ACPD
11, 31159–31206, 2011

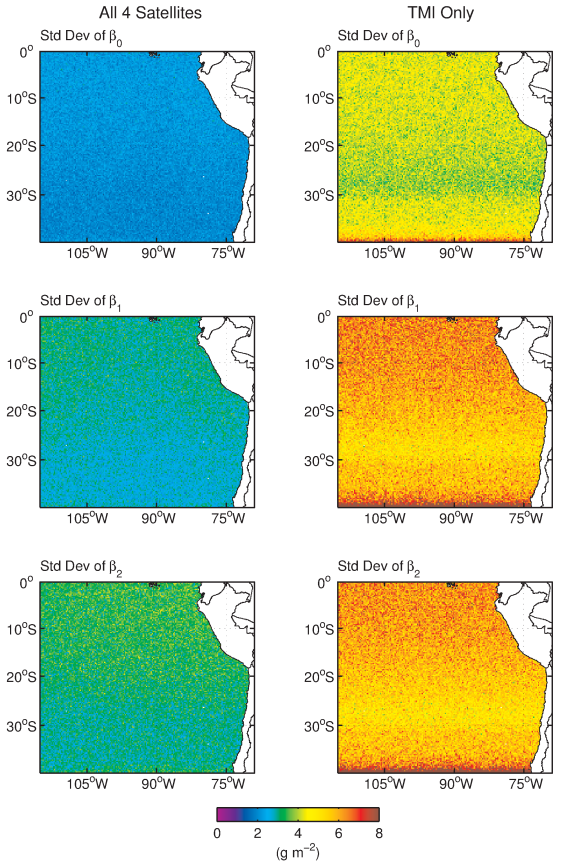

Fig. 6. Maps of the standard deviation of the regression parameters computed from least-squares regression of the synthetic LWP time series for the 7-yr period June 2002–May 2009 at monthly intervals. The regression coefficients were computed from the four-satellite combination in the left column of panels and from the TMI only in the right column of panels.

ACPD
11, 31159–31206, 2011

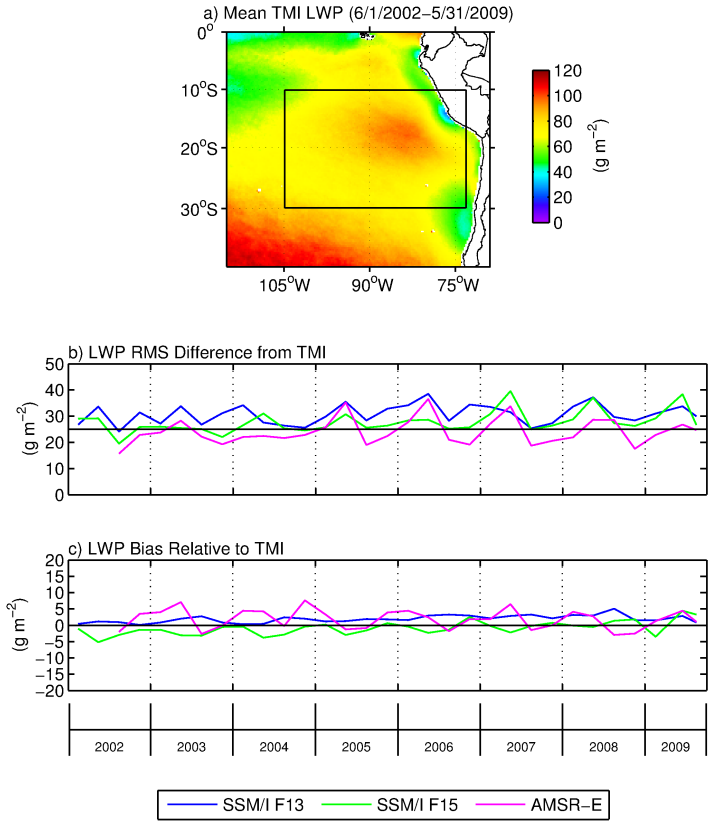

Fig. 7. (a) Map of the 7-yr mean LWP from TMI for the period June 2002–May 2009. **(b)** Time series of the RMS differences of LWP between the TMI and: (red) AMSR-E, (blue) SSM/I F13, and (green) SSM/I F15. **(c)** Same as **(b)**, except for the LWP mean differences. These statistics were computed from measurements taken within ±20 min of the TMI observations at 3-month intervals in the region shown by the rectangle in **(a)**.

ACPD
11, 31159–31206, 2011

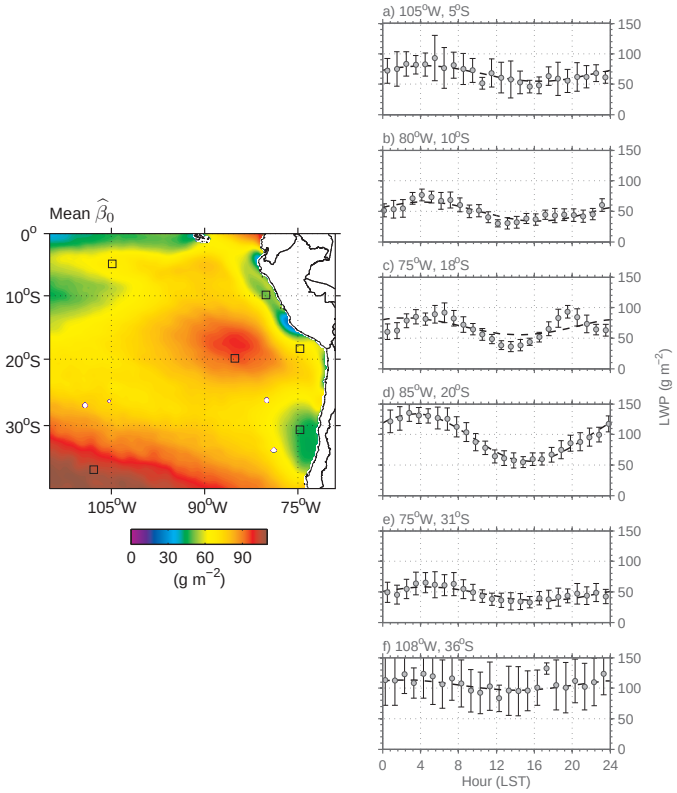

Fig. 8. (Right column) Examples of the LWP diurnal cycle computed from the 7 yr of LWP measured by the four-satellite combination shown by the squares in the accompanying map. The gray points represent the 7-yr LWP in the hourly bins and the error bars represent ±1 standard deviations about the mean. The dashed curves are the mean diurnal regression fits computed from the 7-yr mean regression coefficients. The map at left shows the 7-yr mean $\widehat{\beta}_0$ and is used to give spatial context to the choice of example points.

ACPD
11, 31159–31206, 2011

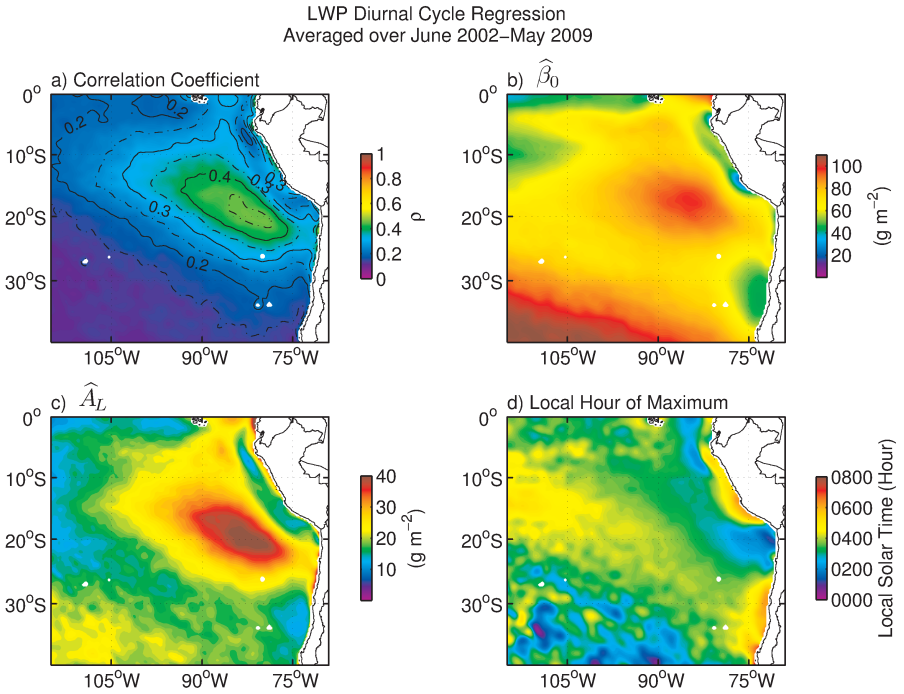

Fig. 9. Maps of the mean LWP diurnal regression variables averaged over the 7-yr period June 2002–May 2009 from the four-satellite combination: **(a)** correlation coefficient computed for each 30-day period and averaged over the 7-yr period; **(b)** $\widehat{\beta}_0$; **(c)** LWP diurnal cycle amplitude $\widehat{A}_L$; and **(d)** LWP diurnal cycle phase $\widehat{P}_L$, which is the time of the peak in the LWP diurnal cycle in LST. The alternating dashed and solid contours in **(a)** are in alternating intervals of 0.05.

ACPD
11, 31159–31206, 2011

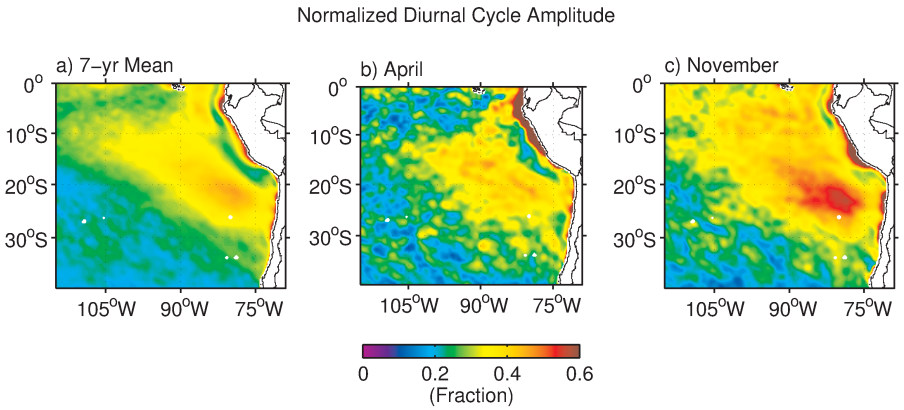

Fig. 10. Maps of the mean LWP diurnal cycle amplitude $\widehat{A}_L$ normalized by the mean $\widehat{\beta}_0$ averaged over: **(a)** the 7-yr analysis period; **(b)** April 2003–2009; and **(c)** November 2002–2008.

ACPD
11, 31159–31206, 2011

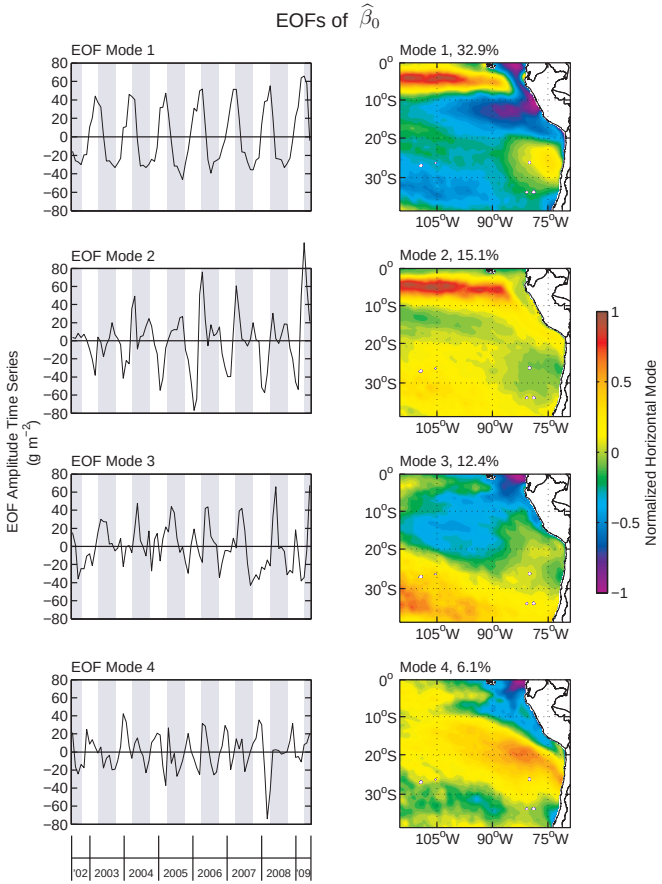

Fig. 11. The four most dominant EOFs of the regression coefficient estimate $\widehat{\beta}_0$. The EOF amplitude time series are shown in the panels on the left, and maps of the EOF normalized spatial modes are shown in the panels on the right. Listed above these maps is the percentage of total variance explained by each mode.

ACPD
11, 31159–31206, 2011

Satellite climatology of cloud liquid water path

L. W. O'Neill et al.

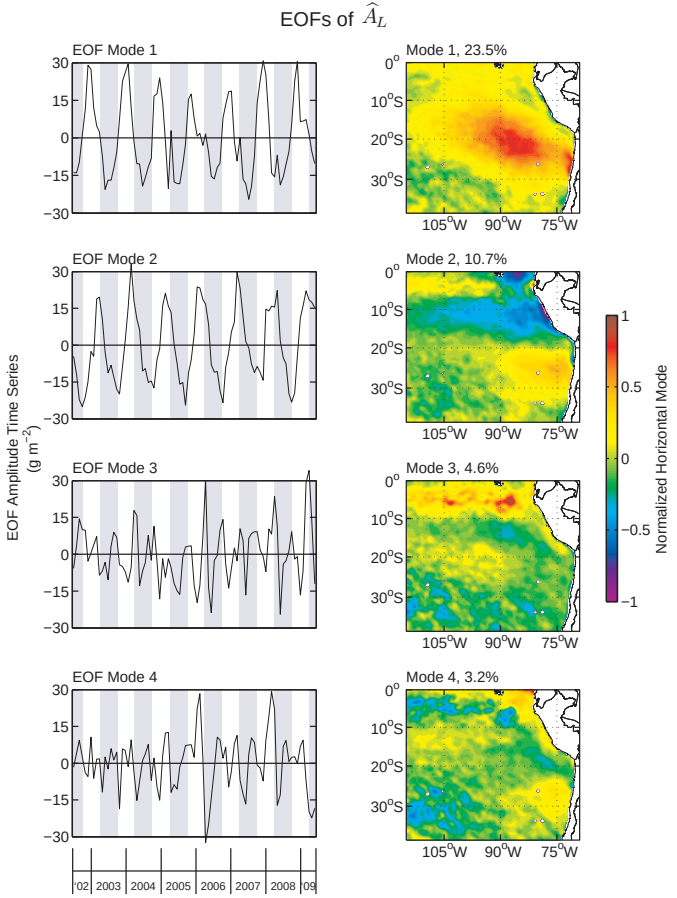

Fig. 12. Same as Fig. 11, except for EOFs of the regression coefficient estimate of the LWP diurnal cycle amplitude $\widehat{A}_L$.

ACPD
11, 31159–31206, 2011

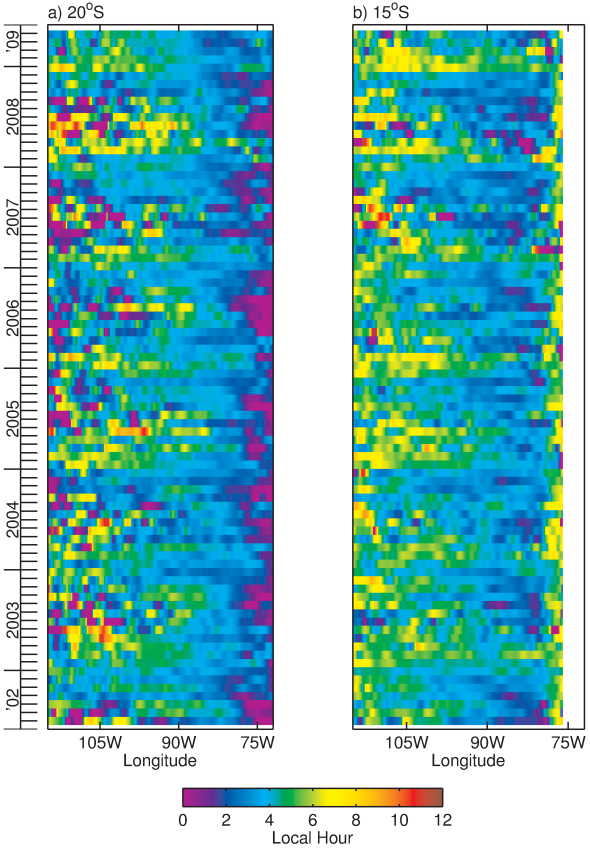

Fig. 13. Time-longitude plot of the diurnal cycle phase in local solar time along **(a)** 20° S and **(b)**15° S.

ACPD
11, 31159–31206, 2011

Satellite climatology of cloud liquid water path

L. W. O'Neill et al.

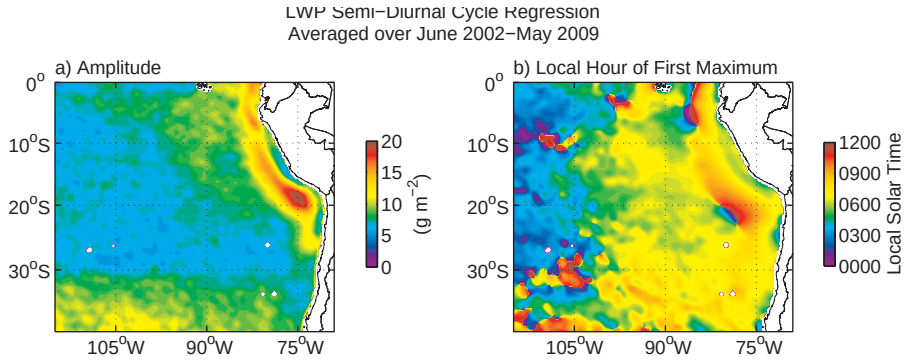

Fig. 14. Maps of the LWP semi-diurnal cycle **(a)** amplitude and **(b)** phase. These were computed similarly to the LWP diurnal cycle discussed earlier.

ACPD
11, 31159–31206, 2011

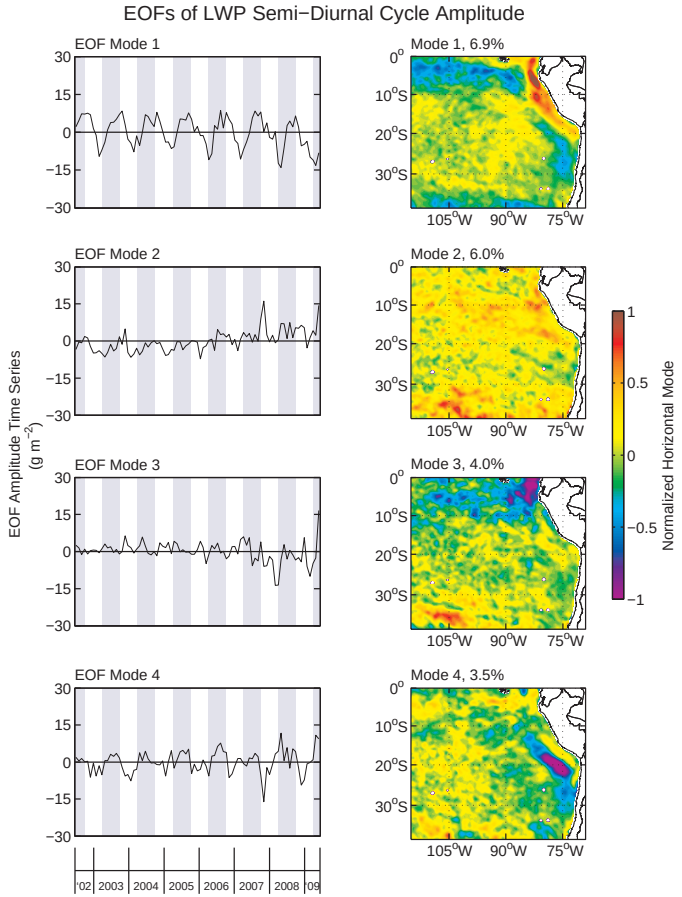

Fig. 15. Same as Fig. 11, except for EOFs of the regression coefficient estimate of the LWP semi-diurnal cycle amplitude.

ACPD
11, 31159–31206, 2011

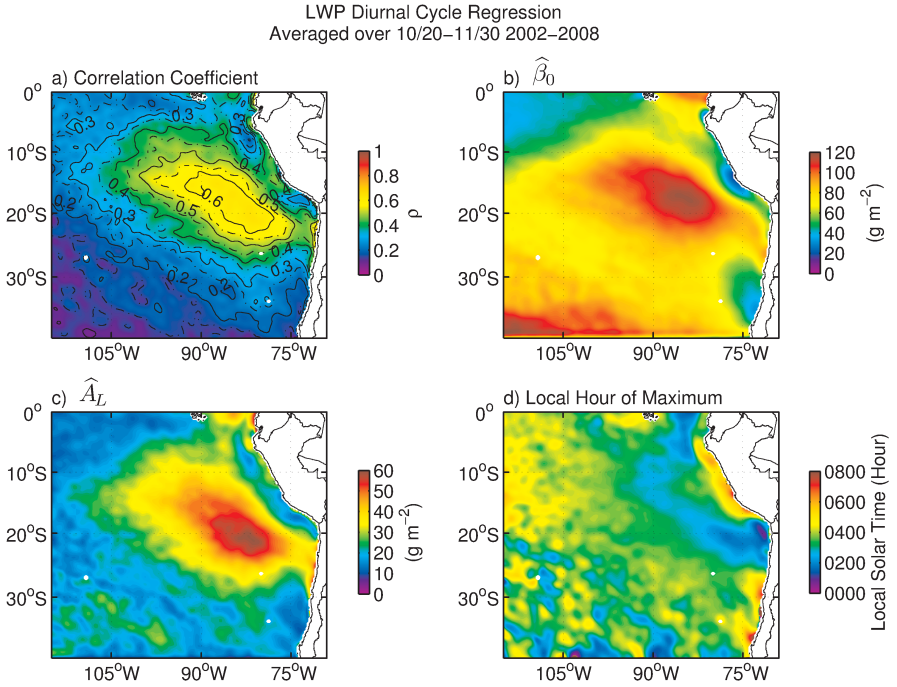

Fig. 16. Maps of the mean LWP diurnal regression variables averaged for 20 October– 30 November 2002–2008 from the four-satellite combination: **(a)** correlation coefficient; **(b)** $\widehat{\beta}_0$; **(c)** LWP diurnal cycle amplitude $\widehat{A}_L$; and **(d)** LWP diurnal cycle phase $\widehat{P}_L$, which is the time of the peak in the LWP diurnal cycle in LST. The alternating dashed and solid contours in **(a)** are in alternating intervals of 0.05.

ACPD
11, 31159–31206, 2011

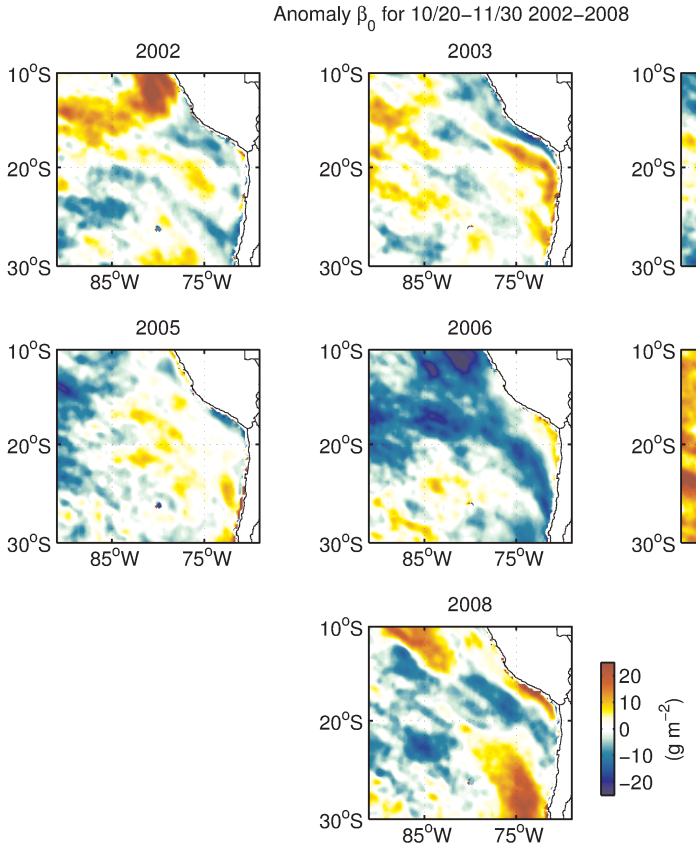

Fig. 17. Maps of β_0 anomalies relative to the mean maps in Fig. 16a over the period 20 October–30 November for the indicated years.

ACPD
11, 31159–31206, 2011

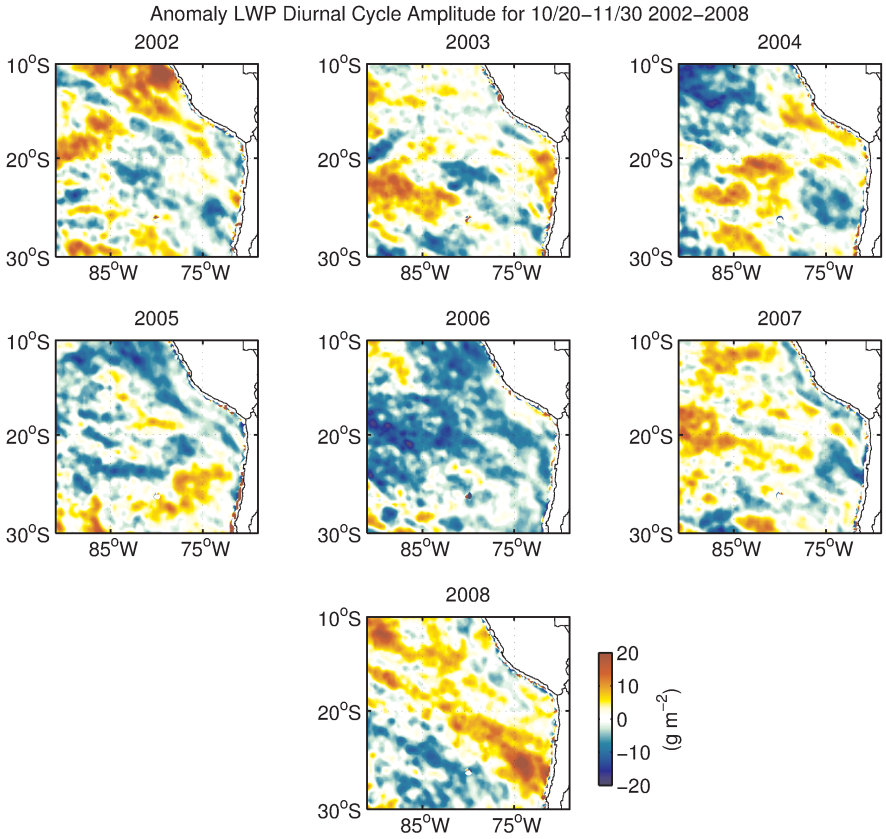

Fig. 18. Maps of LWP diurnal cycle amplitude anomalies relative to the mean amplitude maps in Fig. 16b over the period 20 October–30 November for the indicated years.

ACPD
11, 31159–31206, 2011

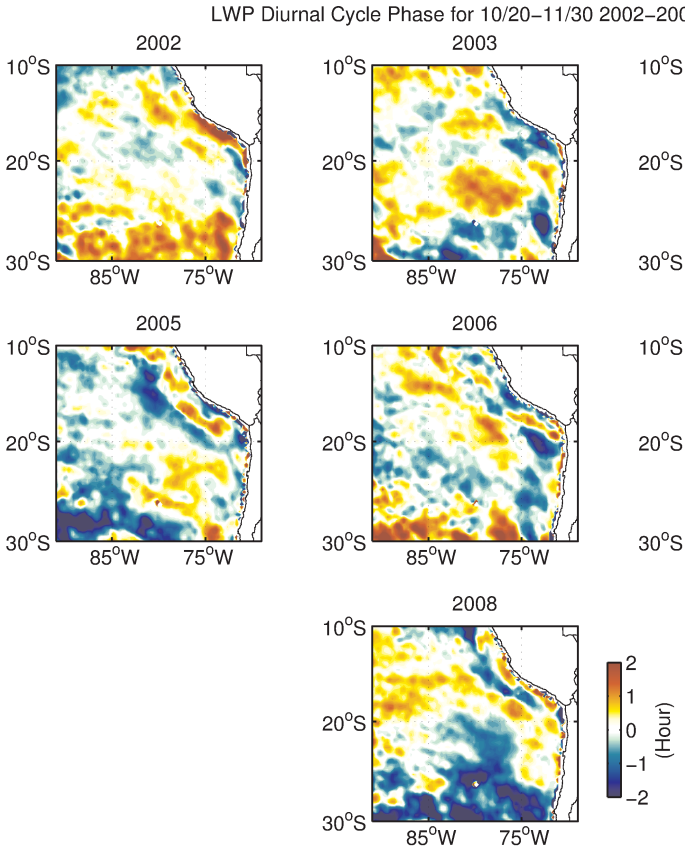

Fig. 19. Maps of LWP diurnal cycle phase anomalies relative to the mean phase maps in Fig. 16d over the period 20 October–30 November for the indicated years.

ACPD
11, 31159–31206, 2011